Robotica (2022), **40**, pp. 1570–1586
doi:10.1017/S0263574721001260

CAMBRIDGE
UNIVERSITY PRESS

RESEARCH ARTICLE

Model-based joint and task space control strategies for a kinematically redundant parallel manipulator

João Vitor de Carvalho Fontes[1], Fernanda Thaís Colombo[2], Natássya Barlate Floro da Silva[3] and Maíra Martins da Silva[2,*]

[1]Federal University of São Carlos, Rod. Washington Luís km 235 - SP-310 - São Carlos, Brazil, [2]São Carlos School of Engineering, University of São Paulo, Av. Trab. São Carlense, 400, São Carlos, Brazil and [3]Federal University of Technology - Paraná, Av. Alberto Carazzai, Cornélio Procópio, Brazil
*Corresponding author. mairams@sc.usp.br

Received: 19 April 2021; **Revised:** 6 August 2021; **Accepted:** 7 August 2021; **First published online:** 7 September 2021

Keywords: parallel kinematic machine; kinematic redundancy; model-based control strategies; experimental results

Abstract

One alternative to overcome the presence of singularities within Parallel Manipulators' workspace is kinematic redundancy. This design alternative can be realized by adding an extra active joint to a kinematic chain. Due to this addition, the IKM presents an infinite number of solutions requiring a redundancy resolution scheme. Moreover, Parallel Manipulators' control may require complex strategies due to their coupled and complex dynamic and kinematic relations. In this work, a model-free, a joint space computed torque, and a hybrid joint-task-space computed torque control strategies are experimentally compared for a kinematically redundant parallel manipulator. The latter is a novel strategy that requires the measurement of the end-effector's pose, which is performed by an eye-to-hand limited frame rate camera. The impact of up to three kinematic redundancy levels is also experimentally evaluated using prepositioning and ongoing positioning redundancy resolution schemes. The data are assessed by evaluating a prescribed trajectory executed using a planar kinematically redundant parallel manipulator. These results indicate that kinematic redundancy can not only be used as an alternative design for reducing the presence of singular regions, as claimed in the literature, but also be used along with model-based control strategies for improving dynamic performance and accuracy of parallel manipulators.

1. Introduction

Static and dynamic features as high load-carrying capacity, rigidity [1], improved dynamic performance [2], and energy efficiency [3] are usually present in Parallel Manipulators. Despite presenting such advantages, the presence of singularities within their limited workspace [4] may jeopardize their industrial applicability. In this way, strategies to overcome this issue demand not only the proposal of innovative kinematic architectures [5,6] but also the usage of rather complex control strategies [7–9].

Among the innovative kinematic architectures, the use of actuation or kinematic redundancies may be a suitable alternative for enlarging the usable workspace [10,11]. In summary, while actuation redundancy can be implemented by the actuation of passive joints or by the inclusion of active kinematic chains, kinematic redundancy can be implemented by introducing extra active joints in a kinematic chain. In particular, kinematically redundant parallel manipulators not only present reconfiguration capabilities for avoiding singular regions but also may present increased accuracy [12,13], higher motion/force transmissibility [14], enhanced dynamic performance [15], and improved energy efficiency [16,17]. Figure 1 shows the 3PRRR, a kinematically redundant planar parallel manipulator. The letter R stands for revolute joint and P for prismatic joint, while the underlined letters represent the active joints. This manipulator presents up to three levels of kinematic redundancy depending on the actuation of the prismatic joints.

© The Author(s), 2021. Published by Cambridge University Press.

https://doi.org/10.1017/S0263574721001260 Published online by Cambridge University Press

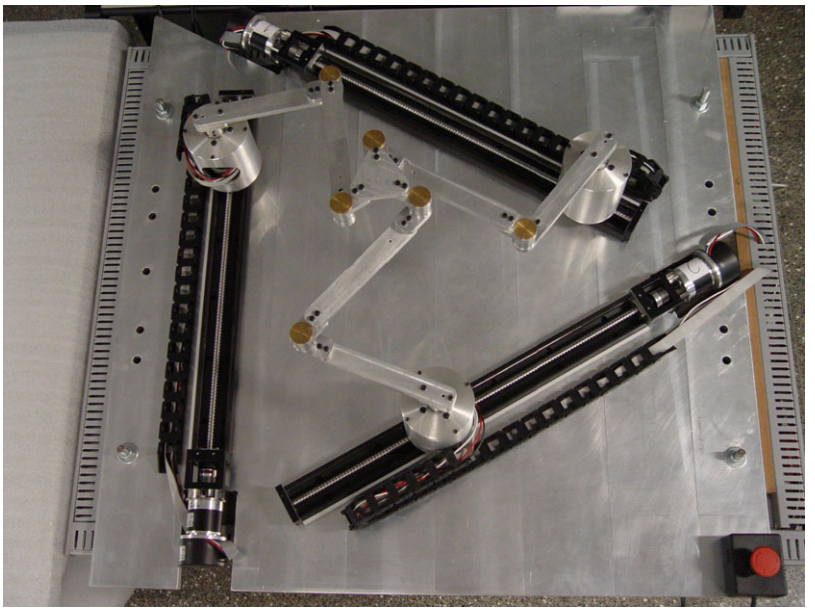


Figure 1. *The prototype 3PRRR: a planar kinematically redundant parallel manipulator.*

The inverse kinematic problem of kinematically redundant manipulators admits infinite solutions. The selection of a single solution requires the use of a redundancy resolution scheme that can be solved locally or globally [18]. Global approaches, also known as tracking problems, are usually employed to derive optimal inputs for a given trajectory of the manipulator's end-effector. Several global approaches have been used for solving redundancy resolution problems in the field of parallel manipulators: heuristic-based iterative methods [19], predictive approaches [16,20], dynamic programming [21], quadratic programming [22], topological analysis [23], among others. Nevertheless, the control of this kind of manipulator can be a challenging task.

The control of parallel manipulators imposes different challenges than their implementation for serial manipulators [24]. For instance, joint space control strategies require the calculation of the inverse kinematic model (IKM). Due to their kinematic architecture, this calculation might be cumbersome and time consuming for parallel manipulators. Alternatively, task-space control strategies require measuring the pose of the manipulator's end-effector that can be done by using vision-based techniques and image processing algorithms [25]. A redundant feedback strategy at the joint and task-space level are proposed by ref. [26] using appropriate sensors. Using this approach, the actual error of the joint displacements are computed, improving the control performance. A similar strategy has been proposed by ref. [27] using a rate-limited camera. However, as highlighted by refs. [24,27], these techniques and algorithms must cope with the required sampling time for avoiding delays in the control loops. Both difficulties might yield a lack of performance and stability issues.

Model-based control strategies, which require the derivation of accurate and computationally efficient dynamic models for avoiding stability and performance issues [28,29], seem to be superior compared to nonmodel ones [8]. These strategies have also been used to overcome the Parallel Manipulators' drawback related to singular regions [30,31]. For instance, Pagis *et al.* [30] propose a multimodel control law that allows parallel manipulators to cross Type 2 singularities, while Nguyen *et al.* [31] propose a novel control approach based on the regularization of singular value decomposition (SVD) to solve the singularity problem. Regarding redundantly actuated parallel manipulators, redundancy introduces an infinite number of actuating torque vectors that would satisfy a given task's requirements. Several model-based control strategies have been proposed to cope with this challenge as reviewed by ref. [32].

https://doi.org/10.1017/S0263574721001260 Published online by Cambridge University Press

For instance, Muller and Hufnagel [11] propose a computed torque and augmented PD control scheme using redundant coordinates.

Regarding kinematically redundant parallel manipulators, fewer studies have been reported. A general framework multipriority controller aiming to minimize the execution time and the overall actuator effort is proposed by ref. [34]. Two joint space control strategies and global redundancy resolution schemes have been experimentally compared in ref. [35]. New insights could be found by evaluating the impact of several levels of kinematic redundancies and different control/redundancy resolution schemes in the field of parallel manipulators. Moreover, not only joint space but also task-space control strategies should be investigated. In this way, this work aims to show that kinematic redundancy can not only be used as an alternative design for reducing the presence of singular regions, as stated in the literature, but also be used along with model-based control strategies for improving dynamic performance and accuracy of parallel manipulators.The evaluation of the impact of several levels of kinematic redundancies and different control/redundancy resolution schemes in parallel manipulators can bring new insights to the field. Moreover, the performance assessment of model-based and model-free control approaches should be addressed. Since their evaluation, along with several kinematic redundancy levels, has not been previously investigated.

In this way, numerical and experimental results on the tracking performance of a planar kinematically redundant parallel manipulator, the 3PRRR (see Fig. 1), are presented and discussed. This performance is assessed by evaluating joint errors, efforts, and repeatability. Three control strategies are evaluated: (i) a nonmodel based joint control strategy (PID), (ii) a model-based joint space CTC, and (iii) a model-based hybrid joint-task computed torque control strategy (HYB). The latter is a novel strategy that requires measuring the end-effector's pose, which is performed by an eye-to-hand limited frame rate camera. Moreover, the impact of up to three kinematic redundancy levels is evaluated using two global redundancy resolution schemes.

The rest of the manuscript is organized as follows. Section 2 describes the prototype and summarizes the kinematic and dynamic models of the manipulator. While Section 3 introduces the investigated redundancy resolution schemes; Section 4 describes the proposed control strategies. Experimental results are presented and discussed in Section 5. Conclusions are drawn in Section 6.

2. 3PRRR: Prototype and Modeling

In this section, the prototype 3PRRR is first described (see Fig. 1). Then, the visual system and image processing technique are introduced. Finally, its kinematic and dynamic models are briefly derived for the sake of completeness. Fontes *et al.* [15] describe these models in detail. The geometric parameters required for the derivation of the kinematic and dynamic models of the 3PRRR manipulator are illustrated in Fig. 2.

2.1. Prototype

Each kinematic chain presents an active prismatic joint (P) and an active revolute joint (R). The actuation of these joints is performed by brushless Maxon EC60 flat motors delivering 100 W of power. These motors are coupled with Maxon planetary gearheads GP52C with a reduction ratio of 3.5:1, resulting in a nominal torque of 0.82 N.m @ 1200 rpm. Table systems with ball screw HIWIN KK60-10-C-E-600-A-1-F0-S3 are responsible for the linear motion. Their stroke range is 600 mm, and their lead is 10 mm. The Maxon EPOS2 50/5 controllers generate the actuation signals and acquire the encoders' measurements. These signals are processed in a DSpace 1103 acquisition board at a rate of 100 *Hz*. The communication between the Maxon EPOS2 50/5 controllers and the DSPACE board is performed using CAN protocol. The torques of the active revolute joints, $\boldsymbol{\tau}_{\theta}$, and the active prismatic joints, $\boldsymbol{\tau}_{\delta}$, are proportional to these actuation signals.

https://doi.org/10.1017/S0263574721001260 Published online by Cambridge University Press

Table I. *Inertial and geometric parameters of the 3PRRR manipulator prototype.*

Parameters	Values	Units	Parameters	Values	Units
l_1	0.191	m	l_2	0.232	m
m_1	0.300	kg	m_2	0.354	kg
I_1	3.640	10^{-3}kg m^2	I_2	6.350	10^{-3}kg m^2
h	0.059	m	a	0.259	m
m_n	0.780	kg	m_0	591.1	kg
I_n	1.470	10^{-5}kg m^2	K	0.01	m

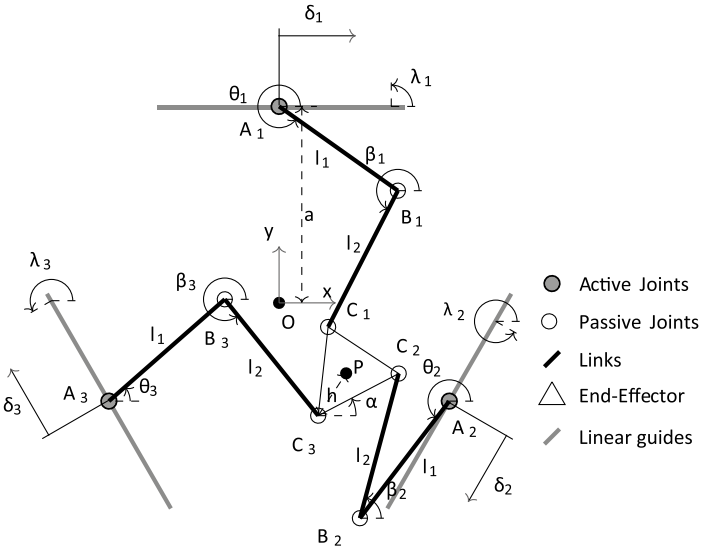


Figure 2. *The geometrical parameters of the 3PRRR.*

In Fig. 2, the subscript $i = 1, \ldots, 3$ indicates the kinematic chain. In each kinematic chain, there are one active (A_i) and two passive (B_i and C_i) revolute joints. The angles θ_i and β_i represent the orientation of the links A_iB_i and B_iC_i, respectively. Their lengths are l_1 and l_2, respectively.

Active prismatic joints can modify the position of the point A_i. By using these linear actuators, the position of A_i can be modified according to the position δ_i and the orientation γ_i ($\gamma_i = \lambda_i - \pi/2$) of the linear guide. The angular position of the active revolute joints, $\boldsymbol{\theta} = [\theta_1, \theta_2, \theta_3]$, are directly acquired by the encoders, while the position of the active prismatic joints, $\boldsymbol{\delta} = [\delta_1, \delta_2, \delta_3]$, can be derived by using the encoders' measurements and the lead values.

The distance between the manipulator's center and the central position of the linear actuators is represented by a. The distance of C_i to the centre of the end-effector is h. The geometric and inertia values are given in Table. I. The inertia values have been obtained using a model identification procedure in a similar way that was proposed by [33]. The following inertia data are used in the dynamic modeling: the mass at the actuator A_i is m_0, the link A_iB_i's mass and moment of inertia around pivot point A_i are m_1 and I_1, the link B_iC_i's mass and moment of inertia around pivot point B_i are m_2 and I_2 and the end effector's mass and moment of inertia around the mass center are m_n and I_n.

2.2. Visual system and image processing tecnique

The hybrid joint-task CTC strategy requires the measurement of the end-effector's pose, $\mathbf{X} = [x, y, \alpha]^T$. This strategy is carried out using a limited frame rate camera and image processing algorithms. In an eye-to-hand configuration, a USB 3.0 oCam-5CRO-U colour camera is placed on top of the manipulator,

https://doi.org/10.1017/S0263574721001260 Published online by Cambridge University Press

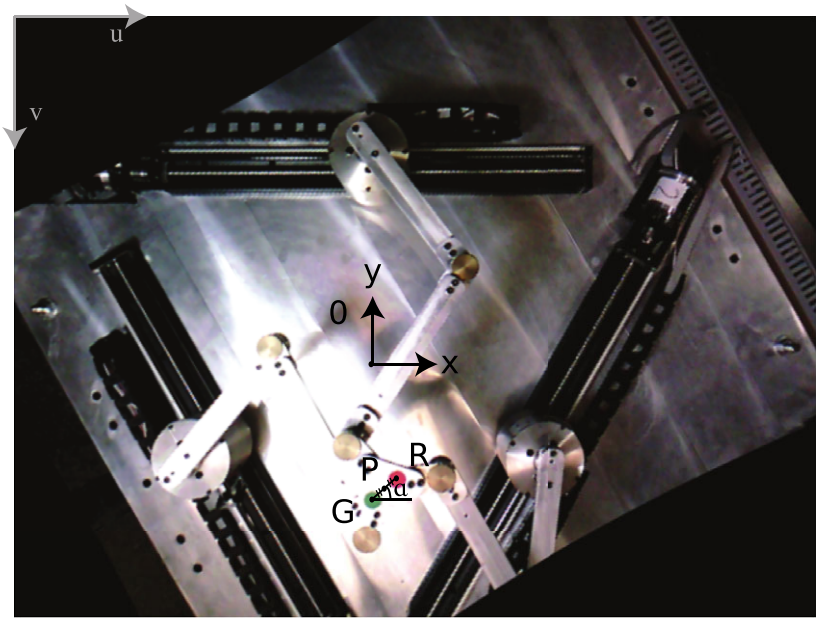


Figure 3. *An image frame used to measure the end-effector's pose based on the detection of the two colored markers and the coordinate transformation between the uv- and xy-axes.*

capturing an image frame that is parallel to the planar workspace. As illustrated in Fig. 3, the red and green markers on the end-effector have a significant color difference compared to the rest of the image. Color segmentation is a simple image processing method that can detect objects of a specific color in the image frame, such as the circular markers used. Most color cameras use the RGB (Red, Green, Blue) color space to represent the colors of the pixels by a combination of Red, Green, and Blue. However, for color filtering of an image, a common approach is the conversion to the HSV (Hue, Saturation and Value) colour space since only the Hue channel is needed to describe the pixel's color. Saturation represents the amount of the color, while Value depends on the lighting conditions. After selecting a range of pixel values in either RGB or HSV color spaces that best describe the color of the object to be detected, the image can be segmented by applying a mask or filter. A binary image with the detected object is created by selecting only the pixels that belong to the range specified.

Two binary images representing the red and green circular markers on the end-effector are extracted. The center of the circles is the average position of all white pixels in each binary image. Geometric relationships between these two points and the end-effector can be used to compute its pose in the image coordinates. The end-effector's center is the average between the center of the green and red markers (see Fig. 3). The angular position is also easily acquired by considering that the markers' centers form a parallel line with one side of the end-effector. Although the end-effector's pose is measured using image-based coordinates, it is possible to convert it into position-based ones, such as the manipulator's reference system. Since the workspace plane is parallel to the image frame, this coordinate transformation only needs a translation of axes, as seen in Fig. 3. To shift the origin between these coordinate systems, we obtained the manipulator's coordinates origin in the image frame in a calibration test. For an undistorted image, the corresponding size of a pixel at the workspace plane is used as a scaling factor between these coordinate systems. This algorithm can measure the end-effector's pose at a sampling time of 60 Hz with an image resolution of 640x480 pixels. Accuracy depends on the relation between in pixel the actual measurement. This is assessed during the system calibration. For the used device, the accuracy is 0.2 mm.

https://doi.org/10.1017/S0263574721001260 Published online by Cambridge University Press

2.3. Kinematic modeling

The IKM is used to determine the active joints inputs $\boldsymbol{\Theta} = [\boldsymbol{\theta} \quad \boldsymbol{\delta}]^T = [\theta_1, \theta_2, \theta_3, \delta_1, \delta_2, \delta_3]^T$ that yield a desired end-effector's pose $\mathbf{X} = [x, y, \alpha]^T$. So, considering that a redundancy resolution scheme will define the values of the redundant actuators' inputs, $\boldsymbol{\delta}$, the inverse kinematics of the manipulator can be derived using the geometrical constraint $\left\| \overrightarrow{B_i C_i} \right\| = l_2$, yielding:

$$e_{i1} + e_{i2} \cos(\theta_i) + e_{i3} \sin(\theta_i) = 0, \tag{1}$$

where $e_{i1} = -2l_1\rho_{yi}$, $e_{i2} = -2l_1\rho_{xi}$ and $e_{i3} = \rho_{xi}^2 + \rho_{yi}^2 + l_1^2 - l_2^2$. The auxiliary variables are defined by $\rho_{xi} = x + h\cos(\alpha + \lambda_i) - \delta_i \cos(\gamma_i) - a\cos(\lambda_i)$ and $\rho_{yi} = y + h\sin(\alpha + \lambda_i) - \delta_i \sin(\gamma_i) - a\sin(\lambda_i)$, where γ_i is the orientation of the prismatic joint in the kinematic chain i which can be calculated as $\lambda_i - \pi/2$.

Using the tangent half-angle substitution, θ_i is employed to solve Eq. (1) for θ_i and can be derived as

$$\theta_i = 2\tan^{-1}\left(\frac{-e_{i1} \pm \sqrt{e_{i1}^2 + e_{i2}^2 - e_{i3}^2}}{e_{i3} - e_{i2}}\right) \quad \text{and} \quad \beta_i = \tan^{-1}\left(\frac{\rho_{yi} - l_1\sin(\theta_i)}{\rho_{xi} - l_i\cos(\theta_i)}\right). \tag{2}$$

According to the signal choice in Eq. (2), these manipulator presents eight possible working modes. In this work, the plus sign is selected for all calculations yielding the working mode illustrates in Fig. 1.

One way to determine the Jacobian matrix $\mathbf{J}$ is by taking the time derivative of the constraint relation described by Eq. (1). The matrix form of this derivation can be written as $\mathbf{A}\dot{\mathbf{X}} = \mathbf{B}\dot{\boldsymbol{\Theta}}$, where the matrices $\mathbf{A}$ and $\mathbf{B}$ can be defined as

$$\mathbf{A} = \begin{bmatrix} a_{11} & a_{12} & a_{13} \\ a_{21} & a_{22} & a_{23} \\ a_{31} & a_{32} & a_{33} \end{bmatrix} \quad \text{and} \quad \mathbf{B} = \begin{bmatrix} b_{11} & 0 & 0 & b_{14} & 0 & 0 \\ 0 & b_{22} & 0 & 0 & b_{25} & 0 \\ 0 & 0 & b_{33} & 0 & 0 & b_{36} \end{bmatrix}, \tag{3}$$

where $a_{i1} = l_2\cos(\beta_i)$, $a_{i2} = l_2\sin(\beta_i)$, $a_{i3} = l_2 h\sin(\beta_i - \lambda_i - \alpha)$, $b_{ii} = l_1 l_2 \sin(\beta_i - \theta_i)$ and $b_{ii+3} = l_2\cos(\beta_i - \gamma_i)$. The Jacobian matrix can be defined as $\mathbf{J} = \mathbf{A}^{-1}\mathbf{B}$.

2.4. Dynamic modeling

The dynamic model of the manipulator is derived in this section using the Newton–Euler formulation and the previously described kinematics. According to Table I, the subscripts $j = 0, 1, 2$ are related to the actuator A_i, link A_iB_i and link B_iC_i, while n is related to the end-effector.

The relation between the generalized efforts $\boldsymbol{\tau} = [\boldsymbol{\tau}_\theta \quad \boldsymbol{\tau}_\delta]^T$ applied by the actuators and the forces and moments on the system are expressed with the Principle of Virtual Work [36]. This relation uses the components of the vector $\mathbf{p}_{ij}$, which are composed by the combination of forces and moment applied on the body j of the chain i; the displacement vector $\mathbf{d}_{ij} = [r_{x_{ij}} \quad r_{y_{ij}} \quad \phi_{ij}]^T$; and the components of the vector $\mathbf{p}_n$ composed by the forces and moment applied on the end-effector. Since the dynamic model is defined using virtual work, it is necessary to obtain Jacobian matrices $\mathbf{K}_{ij}$ for each moving body of the manipulator. The detailed definition for these matrices can be found in [15]. This strategy yields the following relation:

$$\boldsymbol{\tau} = \mathbf{J}^T\mathbf{p_n} + \sum_{i=1}^{3}\sum_{j=0}^{2} \mathbf{K_{ij}}^T\mathbf{p_{ij}}. \tag{4}$$

The vectors $\mathbf{p_{ij}}$ and $\mathbf{p_n}$ can be described:

$$\mathbf{p_{ij}} = \mathbf{Z_{ij}}\begin{bmatrix} \ddot{r}_{x_{ij}} \\ \ddot{r}_{y_{ij}} \\ \ddot{\phi}_{ij} \end{bmatrix} + \mathbf{N_{ij}}\begin{bmatrix} \dot{r}_{x_{ij}} \\ \dot{r}_{y_{ij}} \\ \dot{\phi}_{ij} \end{bmatrix} \quad \text{and} \quad \mathbf{p_n} = \mathbf{Z_n}\begin{bmatrix} \ddot{x} \\ \ddot{y} \\ \ddot{\alpha} \end{bmatrix} \tag{5}$$

https://doi.org/10.1017/S0263574721001260 Published online by Cambridge University Press

where

$$\mathbf{Z_{ij}} = \begin{bmatrix} m_j & 0 & -m_j s_{ij} \sin\phi_{ij} \\ 0 & m_j & m_j s_{ij} \cos\phi_{ij} \\ -m_j s_{ij} \sin\phi_{ij} & m_j s_{ij} \cos\phi_{ij} & I_j \end{bmatrix}, \tag{6}$$

$$\mathbf{N_{ij}} = \begin{bmatrix} 0 & 0 & -m_j \dot{\phi}_{ij} s_{ij} \cos\phi_{ij} \\ 0 & 0 & -m_j \dot{\phi}_{ij} s_{ij} \sin\phi_{ij} \\ 0 & 0 & 0 \end{bmatrix} \quad \text{and} \quad \mathbf{Z_n} = \begin{bmatrix} m_n & 0 & 0 \\ 0 & m_n & 0 \\ 0 & 0 & I_n \end{bmatrix} \tag{7}$$

These equations can be rewritten in term of the time derivatives of $\mathbf{\Theta}$ using the Jacobian matrices yielding:

$$[\tau_1 \quad \tau_2 \quad \tau_3 \quad \tau_4 \quad \tau_5 \quad \tau_6]^T = \mathbf{M}\ddot{\mathbf{\Theta}} + \mathbf{V}\dot{\mathbf{\Theta}}, \tag{8}$$

where:

$$\mathbf{M} = (\mathbf{J}^T \mathbf{Z_n} \mathbf{J} + \sum_{i=1}^{3} \sum_{j=0}^{2} \mathbf{K_{ij}}^T \mathbf{Z_{ij}} \mathbf{K_{ij}}) \quad \text{and} \tag{9}$$

$$\mathbf{V} = (\mathbf{J}^t \mathbf{Z_n} \mathbf{J} + \sum_{i=1}^{3} \sum_{j=0}^{2} \mathbf{K_{ij}}^T \mathbf{Z_{ij}} \mathbf{K_{ij}} + \sum_{i=1}^{3} \sum_{j=0}^{2} \mathbf{K_{ij}}^t \mathbf{N_{ij}} \mathbf{K_{ij}}). \tag{10}$$

Since τ_4, τ_5, and τ_6 are generalized forces, they must be converted to torque using the lead K of the linear guide leading to

$$\boldsymbol{\tau} = [\boldsymbol{\tau}_\theta \quad \boldsymbol{\tau}_\delta]^T = [\tau_1 \quad \tau_2 \quad \tau_3 \quad K\tau_4/(2\pi) \quad K\tau_5/(2\pi) \quad K\tau_6/(2\pi)]^T \tag{11}$$

It is important to highlight that the dynamic model depends on the angles ϕ_{ij}. These angles are defined as 0 for $j = 0$, θ_i for $j = 1$ and β_i for $j = 2$. This dependency is critical for the control strategies based on the model, since β_i can only be analytically calculated by the IKM.

3. Redundancy Resolution

Redundancy resolution is a decision-maker strategy used for deriving the position of the redundant joints among the possibilities. This strategy can be mathematically described as an optimization problem. Some redundancy resolution schemes seek to minimize the maximum required torque to perform a predefined task. However, this approach does not guarantee the avoidance of singular regions during the task execution.

In this work, a multiobjective optimization problem is adopted to overcome this issue. In the proposed approach, the minimization of the required torque is considered and the avoidance of the singular regions. In this way, two functions are defined, υ_1 and υ_2 whose values present a strong relation with the distance from the type 1 and type 2 singularities, respectively. According to Pagis *et al.*, type 1 singularities occur when the mechanism is unable to move in a given direction due to the rank deficiency of the kinematic matrix **B** (Eq. (3)), and type 2 singularities occur when one or more of the manipulator's degrees of freedom become uncontrollable due to the rank deficiency of the kinematic matrix **B** (Eq. (3)). In this way, penalty functions are proposed for guaranteeing the avoidance of types 1 and 2 singularities.

First, a function υ_1 is proposed for the avoidance of type 1 singularities. These singularities can be avoided by assuring that the values of $\sin(\beta_i - \theta_i)$, from Eq. (12), are positive. Equation 12 only considers the nonredundant part of the matrix **B** (see Eq. (3)) in the following way:

$$\mathbf{B}' = \begin{bmatrix} l_1 l_2 \sin(\beta_1 - \theta_1) & 0 & 0 \\ 0 & l_1 l_2 \sin(\beta_2 - \theta_2) & 0 \\ 0 & 0 & l_1 l_2 \sin(\beta_3 - \theta_3) \end{bmatrix}. \tag{12}$$

https://doi.org/10.1017/S0263574721001260 Published online by Cambridge University Press

Considering that the singular values of $\mathbf{B}'$ are related to $\sin(\beta_i - \theta_i)$, the avoidance of type 1 singularity can be guaranteed by maximizing the smallest singular value of $\mathbf{B}'$. Since the smallest singular value varies in time during the task execution, the minimum value of the smallest singular values (worst case) is considered in the optimization problem. In this way, the function υ_1 is defined by

$$\upsilon_1 = min \quad \frac{min\ \nu(\mathbf{B}')}{l_1 l_2}, \tag{13}$$

where $\nu(\mathbf{B}')$ are the singular values of matrix $\mathbf{B}'$, and l_1 and l_2 are used for normalizing the relation. The value of υ_1 varies between 0 and 1 and should be maximized for guaranteeing the avoidance of type 1 singularity.

Second, a function υ_2 is proposed for the avoidance of type 2 singularities. This requirement can be assessed by evaluating indices derived from the Jacobian matrix $\mathbf{A}$ [37]. For the manipulator under study, the Jacobian matrix $\mathbf{A}$ (see Eq. (3)) is not homogeneous and, therefore, the indices defined directly from it have no physical meaning. To overcome this problem, the Jacobian matrix $\mathbf{A}$ could be normalized using the characteristic length of the manipulator, given by $Lc = \sqrt{2}h$ [37,38]. This normalization can be applied to the angular-related elements of the matrix $\mathbf{A}$ yielding the normalized matrix:

$$\mathbf{A}' = \begin{bmatrix} a_{11} & a_{12} & a_{13}/Lc \\ a_{21} & a_{22} & a_{23}/Lc \\ a_{31} & a_{32} & a_{33}/Lc \end{bmatrix}. \tag{14}$$

The distance between the end-effector and the singularities of type 2 is related to the conditioning number of the normalized Jacobian matrix $\mathbf{A}'$ defined by

$$\kappa(\mathbf{A}') = \frac{max\ \nu(\mathbf{A}')}{min\ \nu(\mathbf{A}')}. \tag{15}$$

where $\nu(\mathbf{A}')$ are the singular values of the matrix $\mathbf{A}'$. Since $\kappa(\mathbf{A}')$ varies in time during the task execution, its maximum value is going to be considered in the cost function. In this way, the function υ_2 is defined by

$$\upsilon_2 = max \quad \kappa(\mathbf{A}'). \tag{16}$$

The value of $\nu(\mathbf{A}')$ varies from 1 to ∞. The higher the value of $\nu(\mathbf{A}')$, the nearer to a singularity the end-effect is. In this way, the avoidance of type 2 singularity can be guaranteed by minimizing the υ_2.

The proposed multiobjective optimization problem seeks to minimize the maximum required torque ($\|\boldsymbol{\tau}\|_\infty$), to maximize the function υ_1 for avoiding type 1 singularities and to minimize the function υ_2 for avoiding type 2 singularities. A weighted sum strategy is proposed to convert this multiobjective problem into a single optimization problem defined by

$$F_{cost} = \|\boldsymbol{\tau}\|_\infty + w[\upsilon_2 - \upsilon_1], \tag{17}$$

where w is a weighting factor. The definition of this objective function yields the following nonlinear constrained optimization problem:

$$\begin{aligned} \delta_{i,opt}(t) &= arg \quad min\ _{\delta_i(t)}\ F_{cost} \\ subject\ to: \ & \delta_{min} \le \delta_i(t) \le \delta_{max} \\ & \upsilon_1 \ge R_1 \\ & \upsilon_2 \le R_2 \end{aligned} \tag{18}$$

where R_1 and R_2 are the lower and upper bounds selected to keep the end-effect far enough from the singularities.

The variables of this optimization problem should describe the inputs for the redundant actuators $\delta_i(t)$. Since the inputs $\delta_i(t)$ are time-dependent variables, they cannot be directly used as optimization variables. Thus, two different approaches are explored to represent these variables: prepositioning and ongoing positioning approaches [10].

https://doi.org/10.1017/S0263574721001260 Published online by Cambridge University Press

On the one hand, the prepositioning approach consists of determining the optimal inputs for the redundant active prismatic joints before the execution of the task (the predefined trajectory). In this way, the positions of the active prismatic joints (the linear guides), denoted as $\delta_{fixed_i,opt}$, are the same throughout the execution of the task. Therefore, this optimization problem can be described as

$$\begin{aligned} \delta_{fixed_i,opt} &= arg \quad min\ {}_{\delta_{fixed_i}}\ F_{cost} \\ subject\ to: \ \delta_{min} &\leq \delta_{fixed_i} \leq \delta_{max} \\ \upsilon_1 &\geq R_1 \\ \upsilon_2 &\leq R_2 \end{aligned} \tag{19}$$

On the other hand, the ongoing positioning approach consists of determining the optimal inputs for the redundant active joints considering that they can also move during the execution of the task (the predefined trajectory). A fifth-order polynomial for describing these inputs have been selected. For deriving the coefficients of this polynomial, the initial and final positions, velocities, and accelerations should be known. The initial and final velocities and accelerations are equal to zero. So, the optimization variables are the values of the initial ($\delta_{0_i,opt}$) and final ($\delta_{fi,opt}$) positions of the active prismatic joints (the linear guides). Therefore, this optimization problem can be described as

$$\begin{aligned} [\delta_{0_i,opt}, \delta_{fi,opt}] &= arg \quad min\ {}_{[\delta_{0_i},\delta_{fi}]}\ F_{cost} \\ subject\ to: \delta_{min} &\leq \delta_{0_i} \leq \delta_{max} \\ \delta_{min} &\leq \delta_{fi} \leq \delta_{max} \\ \delta_{min} &\leq \delta_i \leq \delta_{max} \\ \upsilon_1 &\geq R_1 \\ \upsilon_2 &\leq R_2 \end{aligned} \tag{20}$$

Both redundancy resolution schemes are performed offline, which means that they must be executed before the experiment. They are solved by using a hybrid optimization strategy. A classical genetic algorithm (GA) is used for delivering good initial guesses for Sequential Quadratic Programming (SQP), which is responsible for providing refined results. This strategy has been able to provide satisfactory results on reasonable processing time. The outcome of this optimization is the desired positions for the active redundant actuators (the active prismatic joints) which is denoted as $\boldsymbol{\delta}_d(t)$. The values of $\boldsymbol{\delta}_d(t)$ are used as the references for the control strategies.

4. Control Strategies

For a predefined trajectory $\mathbf{X}_d$, a set of desired positions for the active redundant joints $\boldsymbol{\delta}_d$ can be derived by one of the redundancy resolution schemes (Eqs. (19) or (20)). The desired positions of the active nonredundant joints $\boldsymbol{\theta}_d$ can be derived by using the IKM, described in Section 2.3, for given values of $\mathbf{X}_d$ and $\boldsymbol{\delta}_d$. For a given $\boldsymbol{\Theta}_d = [\boldsymbol{\theta}_d \quad \boldsymbol{\delta}_d]^T$, the required torque to be applied in the manipulator is derived using three control strategies in this work. These strategies are experimentally implemented and compared.

The first strategy is a model-free independent PID joint control scheme. This strategy is illustrated in Fig. 4. The desired positions of the active joints, $\boldsymbol{\theta}_d$ and $\boldsymbol{\delta}_d$, are used as reference signals in the control loop. These signals are compared with the actual measurement, $\boldsymbol{\theta}$ and $\boldsymbol{\delta}$, and the differences between these signals, $\boldsymbol{e}_\theta = \boldsymbol{\theta}_d - \boldsymbol{\theta}$ and $\boldsymbol{e}_\delta = \boldsymbol{\delta}_d - \boldsymbol{\delta}$, are the inputs for the PID controls. Different gains are used for the actuators responsible for the motion of the active revolute (nonredundant) and prismatic (redundant) joints. These gains have been experimentally adjusted by a trial-and-error method. The torque calculated using this strategy, $\boldsymbol{\tau}_{PID}$, can be calculated using the following control law:

$$\boldsymbol{\tau}_{PID} = [\boldsymbol{\tau}_\theta, \ \boldsymbol{\tau}_\delta] = K_p \mathrm{e} + K_d \frac{\mathrm{d}e}{\mathrm{d}t} + K_i \int_0^t e \ \mathrm{d}\rho \tag{21}$$

where $\boldsymbol{e} = [\boldsymbol{e}_\theta, \boldsymbol{e}_\delta]$, $\boldsymbol{K}_p$, $\boldsymbol{K}_d$ and $\boldsymbol{K}_i$ are the proportional, derivative and integral gains.

https://doi.org/10.1017/S0263574721001260 Published online by Cambridge University Press

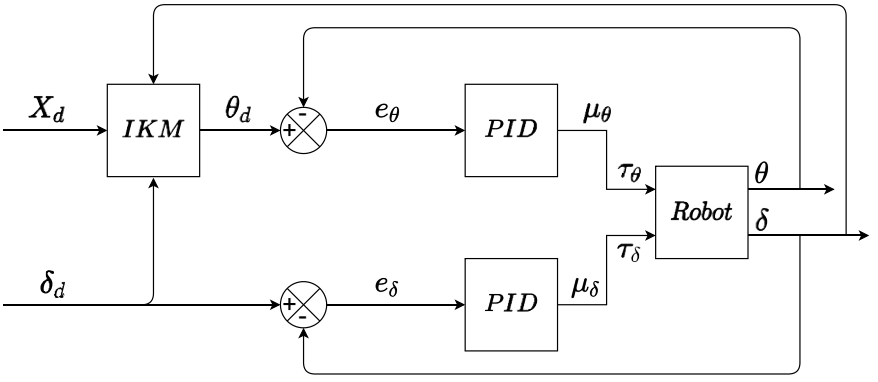


Figure 4. *The independent PID joint control scheme (PID).*

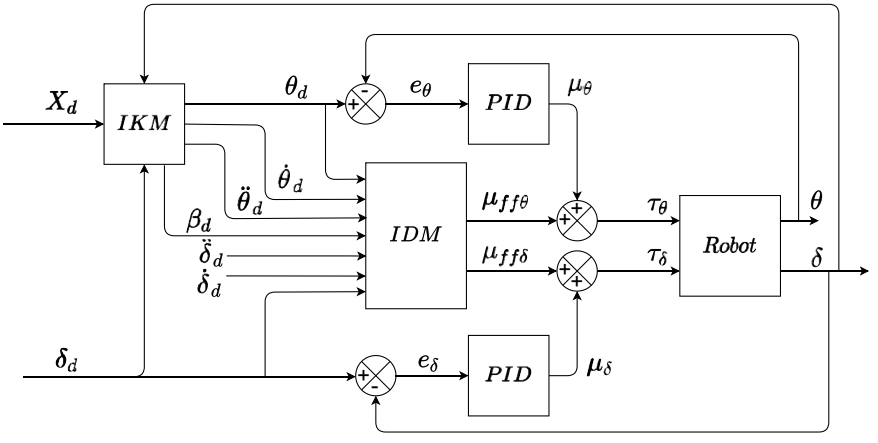


Figure 5. *The CTC strategy.*

The second strategy is a joint space CTC scheme. Figure 5 shows a scheme of the second strategy. In this strategy, a feedforward signal is added since an inverse dynamic model (IDM), derived in Section 2.4, is available. Based on the IKM, the desired joint positions $[\boldsymbol{\theta}_d, \boldsymbol{\delta}_d]$, velocities $[\dot{\boldsymbol{\theta}}_d, \dot{\boldsymbol{\delta}}_d]$ and accelerations $[\ddot{\boldsymbol{\theta}}_d, \ddot{\boldsymbol{\delta}}_d]$ are derived. Moreover, the desired angular positions of the passive joints $\boldsymbol{\beta}_d$ are also derived using Eq. (2). These desired values are used in the Eq. (4) to compute the required torque to the task execution (the feedforward signal):

$$\boldsymbol{\tau}_{ff} = [\boldsymbol{\mu}_{ff\theta},\ \boldsymbol{\mu}_{ff\delta}] = \text{IDM}(\boldsymbol{\beta}_d, \boldsymbol{\theta}_d, \dot{\boldsymbol{\theta}}_d, \ddot{\boldsymbol{\theta}}_d, \boldsymbol{\delta}_d, \dot{\boldsymbol{\delta}}_d, \ddot{\boldsymbol{\delta}}_d) \tag{22}$$

This computed torque (feedforward signal) may enhance the system performance regarding the tracking reference and disturbance rejection capabilities since it might compensate for Coriolis, centrifugal, frictional forces, among others. Nevertheless, the PID scheme is also used in this strategy for robustness since the dynamic model is surely imprecise. This CTC strategy yields the following control law:

$$\boldsymbol{\tau}_{CTC} = [\boldsymbol{\tau}_\theta,\ \boldsymbol{\tau}_\delta] = [\boldsymbol{\mu}_{ff\theta} + \boldsymbol{\mu}_\theta,\ \boldsymbol{\mu}_{ff\delta} + \boldsymbol{\mu}_\delta] \tag{23}$$

where $\boldsymbol{\mu}_\theta$ and $\boldsymbol{\mu}_\delta$ are the output of the PID controllers as can be seen in Fig. 5.

The third strategy is a hybrid joint-task space CTC strategy. Figure 6 shows a scheme of the third strategy. While the computed torque is derived using the desired kinematic quantities (Eq. (22)) in the second control strategy, the actual measurements will be used in the control loops in the third control strategy. Not only the actual positions of the nonredundant and redundant actuators, $\boldsymbol{\delta}$ and $\boldsymbol{\theta}$ (joint space), but also the actual positions of the end-effector, X (task space), are used. The task space is measured using a camera and image processing algorithms (see Section 2.1).

https://doi.org/10.1017/S0263574721001260 Published online by Cambridge University Press

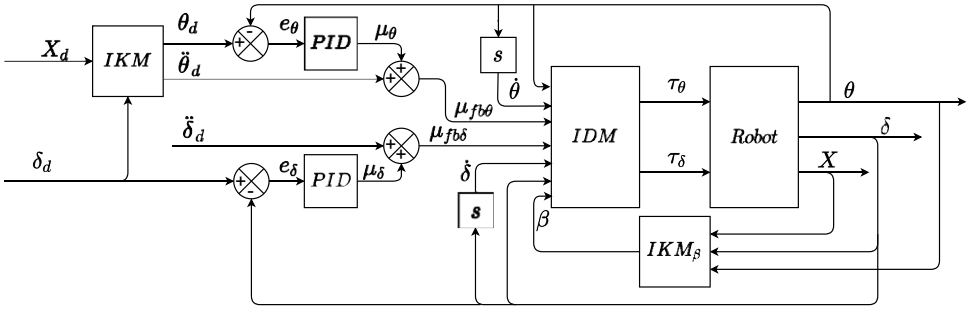


Figure 6. *The Hybrid Joint-Task Space computed torque control strategy (HYB).*

The hybrid joint-task space CTC strategy, illustrated in Fig. 6, presents two control loops: an internal loop that considers the dynamic model and an external loop that tracks the error. For these loops, kinematic quantities are required. The first- and second-time derivatives of the actual actuators' positions are calculated using derivative blocks and estimated signals. The estimated second-time derivative of the nonredundant actuators' positions are calculated by

$$\ddot{\boldsymbol{\theta}}_* = \ddot{\boldsymbol{\theta}}_d + u_\theta \tag{24}$$

where $\boldsymbol{u}_\theta$ is the outcome of PID blocks while the vector of errors of the actuators' positions ($\boldsymbol{e}_\theta = \boldsymbol{\theta}_d - \boldsymbol{\theta}$) is the input. The same approach is used for estimating the second-time derivative of the redundant actuators' positions, $\ddot{\boldsymbol{\delta}}_*$.

The computed torque is calculated using the IDM, which requires not only the actuators' positions but also the angle of the passive joints $\boldsymbol{\beta}$. Using the IKM, the actual angular positions of the passive joints $\boldsymbol{\beta}$ can be also estimated using the actual positions of the active joints, $\boldsymbol{\theta}$, and of the end-effector, X (see Eq. (2)). In this way, these states are used as input signals along with the kinematic quantities of the actuators. In summary, the required torque for executing a task is derived using not only the IKM and the IDM but also the actual and estimated kinematic quantities:

$$\boldsymbol{\tau}_{HYB} = [\boldsymbol{\tau}_\theta,\ \boldsymbol{\tau}_\delta] = \text{IDM}(\boldsymbol{\beta}, \boldsymbol{\theta}, \dot{\boldsymbol{\theta}}, \ddot{\boldsymbol{\theta}}_*, \boldsymbol{\delta}, \dot{\boldsymbol{\delta}}, \ddot{\boldsymbol{\delta}}_*) \tag{25}$$

Both second and third strategies require the calculation of the inertia matrix and the Coriolis vector. These three control strategies are implemented in a Simulink model, compiled for a dSPACE 1103 board. The strategies use the same PID gains for the sake of comparison. In the next section, these strategies are compared considering the RMS (root mean square) of the error vectors ($\boldsymbol{e}_\theta = \boldsymbol{\theta}_d - \boldsymbol{\theta}$ and $\boldsymbol{e}_\delta = \boldsymbol{\delta}_d - \boldsymbol{\delta}$) and the RMS of the torques ($\boldsymbol{\tau}_\theta$ and $\boldsymbol{\tau}_\delta$).

5. Results

In this section, the impact of up to three levels of kinematic redundancy of the planar parallel manipulator 3PRRR is numerically and experimentally evaluated. This evaluation is carried out for two redundancy resolution schemes: the prepositioning approach (PRE - Eq. (19)) and the ongoing positioning approach (ON - Eq. (20)); and for three control strategies: the model-free control (PID - Eq. (21)), the joint space CTC (CTC - Eq. (23)), and the hybrid joint-task space computed torque control (HYB - Eq. (25)) strategies.

For the sake of comparison, the same task is performed for all possible configurations under evaluation. This task is characterized by a point-to-point straight-line trajectory. The initial and the final points are given by $\mathbf{X}_d^{initial} = [0.09\text{ m}, -0.03\text{ m}, 0.2\ rad]$ and $\mathbf{X}_d^{final} = [-0.09\text{ m}, 0.03\text{ m}, 0.1\ rad]$, respectively. The task duration is 1s, and during its execution, the end-effector pass near a singular region. This task is mathematically described using a fifth-degree polynomial considering initial and final velocities and accelerations equal to zero.

https://doi.org/10.1017/S0263574721001260 Published online by Cambridge University Press

Table II. *Maximum torque values, singularities indexes and cost function for the nonredundant and redundant manipulators using different redundancy resolution schemes*

Configuration_active guide	Resolution	$\|\tau\|_\infty$	v_1	v_2	F_{cost}
3RRR	Non	0.2754	2.1359	0.4827	0.3085
PRRR+2RRR_1	Pre positioning	0.2827	2.0522	0.4827	0.3141
PRRR+2RRR_2		0.2895	2.1328	0.5127	0.3219
PRRR+2RRR_3		0.2774	1.9325	0.4827	0.3064
PRRR+2RRR_1	Ongoing positioning	0.2697	2.0000	0.4827	0.3000
PRRR+2RRR_2		0.2863	2.1302	0.5047	0.3189
PRRR+2RRR_3		0.2745	1.8816	0.4827	0.3024
PRRR+RRR_12	Pre positioning	0.2336	2.0000	0.5143	0.2634
PRRR+RRR_13		0.2520	2.0000	0.4827	0.2823
PRRR+RRR_23		0.2497	2.0000	0.4691	0.2803
2PRRR+RRR_12	Ongoing positioning	0.2166	2.0000	0.5757	0.2451
PRRR+RRR_13		0.2487	1.8802	0.4827	0.2766
PRRR+RRR_23		0.2349	2.0000	0.5072	0.2647
PRRR	Pre positioning	0.2072	1.5848	0.6493	0.2259
3PRRR	Ongoing positioning	0.2017	1.5430	0.6240	0.2200

For a given trajectory, $\mathbf{X}_d$, the redundancy resolution schemes are responsible for deriving the inputs for the redundant actuators $\boldsymbol{\delta}_d$. These schemes require the definition of the constraint parameters and weighting factor (Eqs. (19) and (20)). The linear guides must not reach their mechanical limits yielding the following bounds: $\delta_{min} = -0.23$ m and $\delta_{max} = 0.23$ m. The end-effector must stay far enough from the singularities. This can be guaranteed by setting $R_1 = 2$ and $R_2 = 0.45$. Finally, the weighting factor w was defined as 0.02, which prioritizes the minimization of the maximum required torque to perform the trajectory. This choice is carried out from a trial-and-error approach. This prioritization can be applied due to the proper selection of R_1 and R_2. Table II shows the values of the objective functions for the nonredundant and redundant manipulators using different redundancy resolution schemes.

Since the manipulator presents up to three levels of kinematic redundancies, the activation of these redundancies can be done in different ways. For instance, for a single level of kinematic redundancy (PRRR+2RRR), one can activate the linear guide 1 without activating the other two (PRRR+2RRR_1 in Table II), or activate only the linear guide 2 or only the linear guide 3 (PRRR+2RRR_2 and PRRR+2RRR_3, respectively). In the same way, this occurs for two levels of kinematic redundancy, activating the linear guides 1 and 2, or 1 and 3, or 2 and 3 (PRRR+2RRR_12, PRRR+2RRR_13 and PRRR+2RRR_23, respectively). The redundancy resolution schemes have been solved for all possible combinations as shown in Table II.

It can be noted that the lowest objective function value was obtained by the redundant manipulator 3PRRR and the ongoing positioning redundancy resolution scheme. Within each possible combination of redundancy resolution level and scheme, the best configurations are the PRRR+2RRR_3 with prepositioning, the PRRR+2RRR_1 with ongoing positioning, the 2PRRR+RRR_12 with prepositioning and ongoing positioning schemes.

Considering the best configurations within each level and redundancy resolution scheme, it can be noted that the higher the level of kinematic redundancy, the lower the objective function. Comparing the same level of kinematic redundancy, the ongoing positioning redundancy resolution scheme presented a

https://doi.org/10.1017/S0263574721001260 Published online by Cambridge University Press

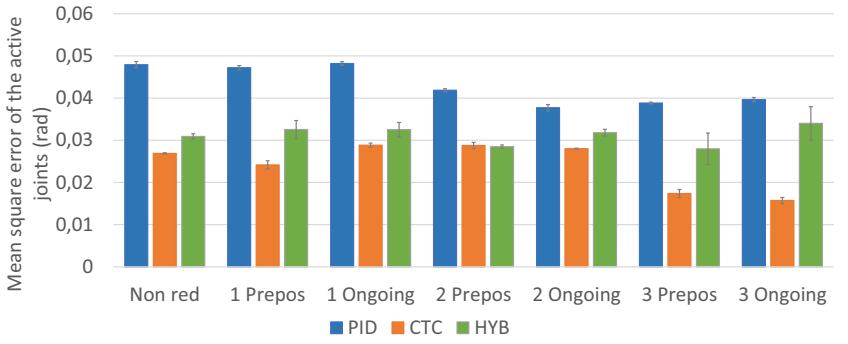


Figure 7. *RMS of $\boldsymbol{e}_\theta$: a comparison between the PID, CTC and HYB control strategies.*

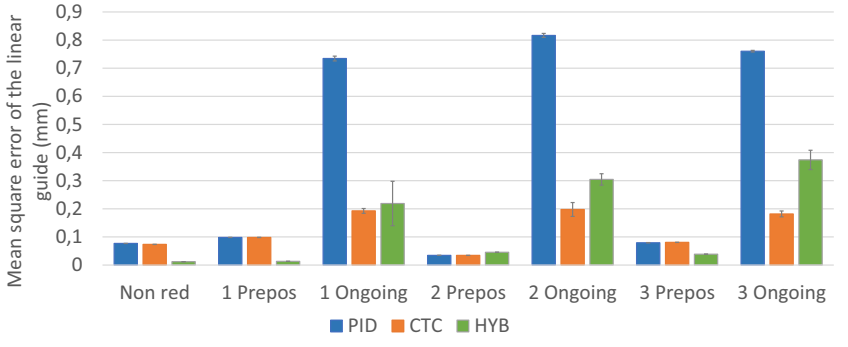


Figure 8. *RMS of $\boldsymbol{e}_\delta$: a comparison between the PID, CTC and HYB control strategies.*

better performance for all configurations. Furthermore, comparing the best case (3PRRR with ongoing positioning) with the worst case (3RRR), there was a reduction of 26% in the maximum torque to perform the same task. In addition, better singularities indices were obtained when three levels of kinematic redundancy were used. This numerical comparison indicates that it is possible to improve the dynamic performance of this manipulator and, at the same time, keep the end-effector away from singularities by using kinematic redundancies.

Based on these numerical results, experiments have been conducted for the configurations presenting the lowest objective function value for each kinematic redundancy level and redundancy resolution scheme. These configurations are highlighted in blue in Table II. In this experimental campaign, the desired trajectory was performed ten times to assess the accuracy of the procedure and improve the reliability of the data. The means and confidence intervals were calculated with a 95 % confidence level.

Figures 7 and 8 show the RMS of $\boldsymbol{e}_\theta$ and $\boldsymbol{e}_\delta$ and their confidence interval for the nonredundant manipulator and for the best configurations of the redundant manipulators. The confidence interval is quite small demonstrating the data accuracy.

The model-based control strategies (CTC and HYB) obtained smaller errors when compared with the model-free control strategy (PID), as shown in Fig. 8. Moreover, the ongoing positioning scheme presented higher errors when used along with the PID control strategy, demonstrating that model-based control strategies deliver superior results for this prototype. Regarding the model-based control strategies, the CTC strategy obtained smaller errors when compared with the HYB strategy. The main reason for this outcome is probably related to the camera rate limitation reducing the control bandwidth of the HYB strategy. Comparing the best case (3PRRR with ongoing positioning scheme and CTC control strategy) with the worst case (3RRR with PID control strategy), there was a reduction of 72 % in the RMS of $\boldsymbol{e}_\theta$ to perform the same task.

https://doi.org/10.1017/S0263574721001260 Published online by Cambridge University Press

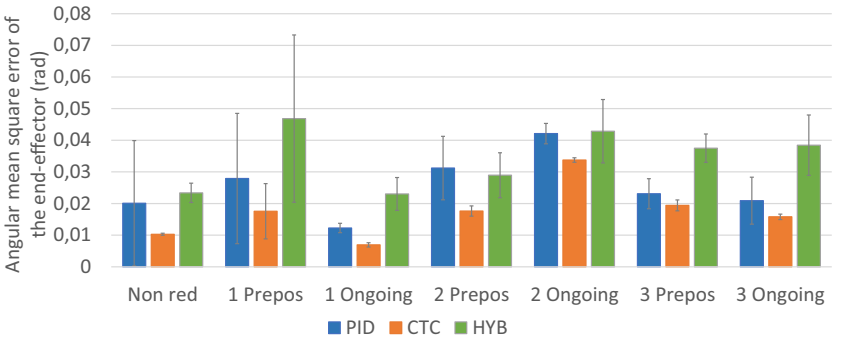


Figure 9. *RMS of the error of the angular postion fo the end-effector ($\alpha_d - \alpha$): a comparison between PID, CTC and HYB control strategies.*

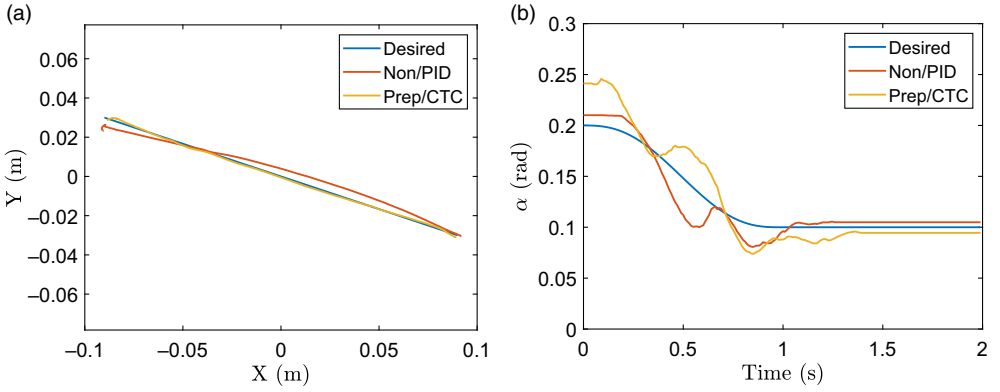


Figure 10. *Comparison between the desired trajectory (desired) and (a) the x and y positions and (b) the α angular position of the end-effector considering the 3RRR/PID control strategy (Non/PID) and the 3PRRR using the prepositioning redundancy resolution scheme/CTC control strategy (Prep/CTC).*

Figure 9 shows the RMS of the error of the angular position of the end-effector ($\alpha_d - \alpha$) and their confidence interval for the nonredundant manipulator and for the best configurations of the redundant manipulators. This figure shows that the error of the end-effector's angular position plays an important role in the total error in the task space. These results might indicate the importance of improving the measurements of the task space for further enhancing the prototype's accuracy. This can also be observed in Fig. 10. This figure shows the x-y and α values of the desired trajectory, the trajectory performed by the 3RRR with PID control strategy (Non/PID), and the trajectory performed by the 3PRRR with prepositioning redundancy resolution scheme and CTC control strategy (Prep/CTC). One can observe that both strategies could guarantee the desired angular position of the end-effector at the end of the task execution (1 s). Moreover, it is important to notice that gravitational forces in both control schemes cause a steady error.

Figure 11 shows the maximum absolute of $\boldsymbol{\tau}$ and confidence interval for the nonredundant manipulator and the best configurations of the redundant manipulators. One can realize that a substantial reduction of the maximum required torque could be achieved by using two or three levels of kinematic redundancy and model-based control strategies. Both redundancy resolution schemes were capable of promoting this reduction. The most significant decrease was achieved by two levels of kinematic redundancies using the prepositioning redundancy resolution scheme. The main reason for this outcome is probably related to the differences between friction coefficients of the linear guides. Comparing the best case (2PRRR+RRR_12 with ongoing positioning scheme and CTC control strategy) with the worst case

https://doi.org/10.1017/S0263574721001260 Published online by Cambridge University Press

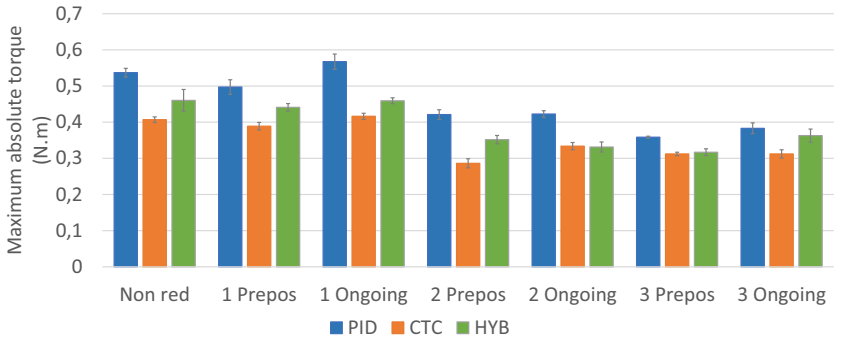


Figure 11. *Maximum absolute of $\boldsymbol{\tau}$: a comparison between the PID, CTC and HYB control strategies.*

(3RRR with PID control strategy), there was a reduction of 47 % in the maximum torque to perform the same task.

These experimental results indicate that it is possible to improve the dynamic performance and, at the same time, improve the task-space accuracy of this manipulator by using kinematic redundancies and model-based control strategies.

6. Conclusions

In this work, the impact of up to three levels of kinematic redundancy of the planar parallel manipulator 3PRRR is numerically and experimentally evaluated. This evaluation is carried out for two redundancy resolution schemes: the prepositioning and the ongoing positioning approaches and for three control strategies: the model-free control, the joint space CTC, and the hybrid joint-task space CTC strategies.

Due to the presence of kinematic redundancies, several configurations could be investigated by activating the redundant actuators. Both redundancy resolution schemes have been numerically investigated for all possible configurations. The same task has been simulated for the sake of comparison. The numerical results indicated that the ongoing strategy applied for the 3PRRR was capable of reducing the maximum required torque by 26% when compared with the nonredundant manipulator. This numerical result indicates that it is possible to improve the dynamic performance of this manipulator and, at the same time, keep the end-effector away from singularities by using kinematic redundancies.

Based on these numerical results, experiments have been conducted for the configurations presenting the lowest objective function value for each kinematic redundancy level and redundancy resolution scheme. The experimental results showed that a reduction of 72% in the RMS value of the end-effector's tracking error was achieved by using the ongoing positioning redundancy resolution scheme for the 3PRRR along with the joint space CTC strategy. Moreover, the experimental results showed that a reduction of 47% in the maximum required torque was achieved using the ongoing positioning redundancy resolution scheme for the 2PRRR+RRR along with the joint space CTC strategy.

These numerical and experimental results indicate that it is possible to improve not only the dynamic performance but also the task-space accuracy of this manipulator by using extra levels of kinematic redundancies and model-based joint and task space control strategies. It is important to highlight that this conclusion should be further investigated by evaluating other trajectory and performance indexes.

Finally, it was expected that the hybrid joint-task space CTC strategy would present the best results because it explores the actual positions of the joints. However, some limitations have been identified by the use of a limited rate-frame camera. The hybrid joint-task space CTC strategy could be improved for future works if an appropriate rate-frame camera is used. Moreover, the accuracy can be further enhanced if strategies for avoiding gravitational errors were applied.

https://doi.org/10.1017/S0263574721001260 Published online by Cambridge University Press

Acknowledgments. This research is supported by FAPESP 2018/21336-0 and CNPq 405569/2016-5. Moreover, Maíra M. da Silva, Fernanda T. Colombo, and Joao V. C Fontes are grateful for their research grants, CNPq 301338/2018-3, FAPESP 2018/22760-0, and CNPq 140561/2015-3, respectively. Natassya Silva acknowledges the support granted by UTFPR.

Competing Interests. The authors declare none.

References

[1] J.-P. Merlet, *Parallel Robots* (Springer, Netherlands, 2006).
[2] O. Company, F. Pierrot, S. Krut, C. Baradat and V. Nabat, "Par2: A spatial mechanism for fast planar two-degree-of-freedom pick-and-place applications," *Meccanica* **46**(1), 239–248 (2011). doi: 10.1007/s11012-010-9413-x
[3] Y. Li and G. M. Bone, "Are Parallel Manipulators More Energy Efficient?," *Proceedings 2001 IEEE International Symposium on Computational Intelligence in Robotics and Automation (Cat. No.01EX515)*, Banff, AB, Canada (2001) pp. 41–46. doi: 10.1109/CIRA.2001.1013170.
[4] C. Gosselin and J. Angeles, "Singularity analysis of closed-loop kinematic chains," *IEEE Trans. Robot. Automat.* **6**(3), 281–290 (1990). doi: 10.1109/70.56660
[5] E. J. Haug, "Parallel manipulator domains of singularity free functionality," *Mech. Des. Struct. Mach,* 1–25 (2020). doi: 10.1080/15397734.2020.1728547
[6] X. Chen and J. Guo, "Effects of spherical clearance joint on dynamics of redundant driving spatial parallel mechanism," *Robotica,* 1–17 (2020). doi: 10.1017/S0263574720000909
[7] A. T. Azar, Q. Zhu, A. Khamis and D. Zhao, "Control design approaches for parallel robot manipulators: a review," *Int. J. Model. Ident. Cont.* **28**(3), 199 (2017). doi: 10.1504/IJMIC.2017.10007051
[8] H. Saied, A. Chemori, M. E. Rafei, C. Francis and F. Pierrot, "From Non-sModel-Based to Model-Based Control of PKMs: A Comparative Study," In: *Mechanism, Machine, Robotics and Mechatronics Sciences*(2018) pp. 153–169. Springer International Publishing.
[9] X. Song, Y. Zhao, C. Chen, L. Zhang and X. Lu, "A PD computed torque control method with online self-gain tuning for a 3UPS-PS parallel robot," *Robotica*, 1–13 (2021). doi: 10.1017/S0263574720001368
[10] J. Kotlarski, H. Abdellatif, T. Ortmaier and B. Heimann, "Enlarging the Useable Workspace of Planar Parallel Robots Using Mechanisms of Variable Geometry," In: 2009 ASME/IFToMM International Conference on Reconfigurable Mechanisms and Robots, London, UK (2009) pp. 63–72.
[11] A. Müller and T. Hufnagel, "Model-based control of redundantly actuated parallel manipulators in redundant coordinates," *Robot. Autonom. Syst.* 60(4), 563–571 (2012). doi: 10.1016/j.robot.2011.11.014.
[12] J. Kotlarski, B. Heimann and T. Ortmaier, "Experimental Validation of the Influence of Kinematic Redundancy on the Pose Accuracy of Parallel Kinematic Machines," In: 2011 *IEEE International Conference on Robotics and Automation* Shanghai, China (2011) pp. 1923–1929. doi: 10.1109/ICRA.2011.5980056.
[13] Y. Jiang, T. Li, L. Wang and F. Chen, "Improving tracking accuracy of a novel 3-DOF redundant planar parallel kinematic machine," *Mech. Mach. Theory* **119**, 198–218 (2018). doi: 10.1016/j.mechmachtheory.2017.09.012.
[14] F. Xie, X.-J. Liu and J. Wang, "Performance evaluation of redundant parallel manipulators assimilating motion/force transmissibility," *Int. J. Adv. Robot. Syst.* **8**(5), 113–124 (2011). doi: 10.5772/50904
[15] J. V. C. Fontes and M. M. da Silva, "On the dynamic performance of parallel kinematic manipulators with actuation and kinematic redundancies," *Mech. Mach. Theory* **103**, 148–166 (2016). doi: 10.1016/j.mechmachtheory.2016.05.004
[16] A. G. Ruiz, J. C. Santos, J. Croes, W. Desmet and M. M. da Silva, "On redundancy resolution and energy consumption of kinematically redundant planar parallel manipulators," *Robotica*, **36**(6), 809–821 (2018). doi: 10.1017/s026357471800005x.
[17] B. N. R. Abadi, M. Mahzoon and M. Farid, "Singularity-free trajectory planning of a 3-RPRR planar kinematically redundant parallel mechanism for minimum actuating effort," *(2019) Iran. J. Sci. Technol. Trans. Mech. Eng.* 43(4), 739–751 (2019). doi: 10.1007/s40997-018-0234-1
[18] B. Siciliano, "Kinematic control of redundant robot manipulators: A tutorial," *J. Intell. Robot. Syst.* **3**(3), 201–212 (1990). doi: 10.1007/bf00126069
[19] J. V. C. Fontes, J. C. Santos and M. M. da Silva, "Numerical and experimental evaluation of the dynamic performance of kinematically redundant parallel manipulators," *J. Braz. Soc. Mech. Sci. Eng.* **40**(3), 142 (2018). doi: 10.1007/s40430-018-1072-1
[20] M. Faroni, M. Beschi, L. M. Tosatti and A. Visioli, "A predictive approach to redundancy resolution for robot manipulators," *IFAC-Papers OnLine* **50**(1), 8975–8980 (2017). doi: 10.1016/j.ifacol.2017.08.1324.
[21] J. C. Santos and M. M. da Silva, "Redundancy resolution of kinematically redundant parallel manipulators via differential dynamic programing," *J. Mech. Robot.* **9**(4), 041016 (2017) doi: 10.1115/1.4036739.
[22] A. Hassan, M. El-Habrouk and S. Deghedie, "Inverse kinematics of redundant manipulators formulated as quadratic programming optimization problem solved using recurrent neural networks: A review," *Robotica* **38**(8), 1495–1512 (2020). doi: 10.1017/S0263574719001590
[23] E. Ferrentino and P. Chiacchio, "On the optimal resolution of inverse kinematics for redundant manipulators using a topological analysis," *ASME. J. Mech. Robot.* **12**(3), 031002 (2020). doi: 10.1115/1.4045178
[24] F. Paccot, N. Andref and P. Martinet, "Review on the dynamic control of parallel kinematic machines: Theory and experiments," *Int. J. Robot. Res.* **28**(3), 395–416 (2009). doi: 10.1177/0278364908096236.

https://doi.org/10.1017/S0263574721001260 Published online by Cambridge University Press

[25] S. Bellakehal, N. Andreff, Y. Mezouar and M. Tadjine, "Vision/force control of parallel robots," *Mech. Mach. Theory* **46**(10), 1376–1395 (2011). doi: 10.1016/j.mechmachtheory.2011.05.010.
[26] S. Mohan, J. K. Mohanta, M. Huesing and B. Corves, "Dual-Loop Motion Control for Geometric Errors and Joint Clearances Compensation of a Planar 2PRP+1PPR Manipulator," *In: Mechanisms, Transmissions and Applications* (2017) pp. 171–180. Springer International Publishing.
[27] F. T. Colombo, J. V. C. Fontes and M. M. da Silva, "A visual servoing strategy under limited frame rates for planar parallel kinematic machines," *J. Intell. Robot. Syst.* **96**(1), 95–107 (2019). doi: 10.1007/s10846-019-00982-7.
[28] P. Di Lillo, G. Antonelli and C. Natale, "Effects of dynamic model errors in task-priority operational space control," *Robotica*, 1–12 (2021). doi: 10.1017/S0263574720001411.
[29] A. Coutinho A. and T. Hess-Coelho, "Improving the performance of parallel robots by applying distinct hybrid control techniques," *Robotica*, 1–25 (2021). doi: 10.1017/S0263574721000874.
[30] G. Pagis, N. Bouton, S. Briot and P. Martinet, "Enlarging parallel robot workspace through type-2 singularity crossing," *Cont. Eng. Pract.* **39** 1–11 (2015). doi: 10.1016/j.conengprac.2015.01.009.
[31] K. T. Nguyen, M. C. Hoang, G. Go, B. Kang, E. Choi, J.-O. Park and C.-S. Kim, "Regularization-based independent control of an external electromagnetic actuator to avoid singularity in the spatial manipulation of a microrobot," *Cont. Eng. Pract.* 97, 104340 (2020). doi: 10.1016/j.conengprac.2020.104340.
[32] M. Luces, J. K. Mills and B. Benhabib, "A review of redundant parallel kinematic mechanisms," *J. Intell. Robot. Syst. Theory Appl.* **86**, 175–198 (2017). doi: 10.1007/s10846-016-0430-4.
[33] T. D. Thanh, J. Kotlarski, B. Heimann and T. Ortmaier, "Dynamics identification of kinematically redundant parallel robots using the direct search method," *Mech. Mach. Theory*, **59**, 277–295 (2012). doi: 10.1016/j.mechmachtheory.2012.02.002
[34] E. Uzunoglu, E. Tatlicioglu and M. Dede, " A multi-priority controller for industrial macro-micro manipulation," *Robotica* **39**(2), 217–232 (2021). doi: 10.1017/S0263574720000338
[35] J. V. C. Fontes, N. B. F. da Silva and M. M. da Silva, "Feedforward Control for the Kinematically Redundant Manipulator 3PRRR," In: *Advances in Mechanism and Machine Science* (2019) pp. 2119–2128. Springer International Publishing. doi: 10.1007/978-3-030-20131-9-210.
[36] J. Wu, J. Wang and Z. You, "A comparison study on the dynamics of planar 3-DOF 4-RRR, 3-RRR and 2-RRR parallel manipulators," *Robot. Comput. Integr. Manufact.* **27**(1), 150–156 (2011). doi: 10.1016/j.rcim.2010.07.001
[37] O. Alba-Gomez, P. Wenger and A. Pamanes, "Consistent Kinetostatic Indices for Planar 3-DOF Parallel Manipulators, Application to the Optimal Kinematic Inversion," In: *29th Mechanisms and Robotics ASME Conference, Parts A and B*, vol. 7 (2005) pp. 765–774. doi: 10.1115/DETC2005-84326.
[38] R. D. Reveles, J. A. Pamanes and G. P. Wenger, "Trajectory planning of kinematically redundant parallel manipulators by using multiple working modes," *Mech. Mach. Theory* **98**, 216–230 (2016). doi: 10.1016/j.mechmachtheory.2015.09.011.

Cite this article: J. V. C. Fontes, F. T. Colombo, N. B. F. da Silva and M. M. da Silva (2022). "Model-based joint and task space control strategies for a kinematically redundant parallel manipulator", Robotica **40**, 1570–1586. https://doi.org/10.1017/S0263574721001260

https://doi.org/10.1017/S0263574721001260 Published online by Cambridge University Press